

1 Theory

1.1 Physical properties of the NV defect center

In the rapidly growing field of quantum computing, it is crucial to realise qubits which ideally avoid any interaction with the environment and consequently don't experience decoherence. As the nitrogen-vacancy-center has proven to achieve extraordinary coherence times even at room temperature, it has become a subject of increasing interest in quantum information processing, especially since its spin state can be optically initialized and read out.

A nitrogen-vacancy-center consists of a nitrogen atom (N) replacing a carbon atom, which is located next to a vacancy (V) in the diamond crystal lattice. There have been found two different types of NV-centers so far: the neutral NV^0 state and the negatively charged NV^- state where an additional electron is captured from the diamond lattice. Due to its well-known and useful optical properties, only latter has been the subject of interest in this work. Therefore it will just be referred to as NV in the following.

The NV properties can be best described with a three-level system. It has a spin triplet ground state 3A whose $m_s = 0$ and $m_s = \pm 1$ sublevels are separated by $D = 2.87$ GHz when no magnetic field is applied. Through spin-conserving, optical transitions, the NV defect can get to the excited spin triplet state 3E . After being excited, it can either relax on the same way, producing broadband photoluminescence (PL) with a zero-phonon line at 637 nm, or without radiation through a secondary path via an intermediate singlet state 1A . The so-called intersystem crossings (ISCs) to the singlet state are strongly spin selective as they involve much more transitions from the $m_s = \pm 1$ sublevels than from $m_s = 0$. Furthermore, from the 1A state, the decay rate to the $m_s = 0$ sublevel is much higher than to $m_s = \pm 1$. Thus, optical pumping allows a high degree of $m_s = 0$ spin polarization. As ISCs are non-radiative, the PL intensity is highest for the pure $m_s = 0$ state and decreases when the defect is driven to $m_s = \pm 1$, so a measurement of the PL provides information about the spin state. Consequently, if a resonant magnetic field is applied to an optically pumped NV, one observes a drop in PL intensity, as can be seen in picture... Furthermore, when the NV is placed in a static magnetic field, the Zeeman effect leads to a lifting of the $m_s = \pm 1$ degeneracy, resulting in two resonance lines in the ESR spectrum. This makes it also possible to use an NV as a magnetic sensor on an atomic scale.

Another striking property is its single photon character which makes it useful in quantum computation and quantum cryptography and allows us to identify an NV using a photon correlation setup. A typical autocorrelation measurement is depicted in picture...

1.2 Bloch notation

An arbitrary state of a two-level system can be written as

$$|\psi\rangle = \alpha|1\rangle + \beta|0\rangle = \alpha \begin{pmatrix} 1 \\ 0 \end{pmatrix} + \beta \begin{pmatrix} 0 \\ 1 \end{pmatrix} = \begin{pmatrix} \alpha \\ \beta \end{pmatrix} \quad (1)$$

Taking into account the normalization condition $\langle\psi|\psi\rangle = |\alpha|^2 + |\beta|^2 = 1$, and neglecting a global phase without physical significance, one can rewrite this as

$$|\psi\rangle = \cos\frac{\theta}{2}|1\rangle + e^{i\phi}\sin\frac{\theta}{2}|0\rangle \quad (2)$$

by introducing the angles θ and ϕ . Thus, an arbitrary state can be represented as a point on a 3D unit sphere, the Bloch sphere, or equivalently as a 3D unit vector, the Bloch vector.

This notation will be used in the following to describe spin manipulations.

1.3 Rabi Oscillations

Let E_0 and E_1 be the corresponding energies to the ground state $|0\rangle$ and the excited state $|1\rangle$. Working in the basis of the two eigenstates, the unperturbed Hamiltonian can be written as

$$\hat{H}_0 = \begin{pmatrix} E_1 & 0 \\ 0 & E_0 \end{pmatrix} = \frac{\hbar\omega_{10}}{2}\hat{\sigma}_z \quad (3)$$

with $\hbar\omega_{10} = E_1 - E_0$. If the system is placed in a classical magnetic field of the form [1]

$$\hat{B} = B_0\hat{e}_z + B_1(\hat{x}\cos\omega t - \hat{y}\sin\omega t) \quad (4)$$

the interaction Hamiltonian reads

$$\hat{H}_B = -\hat{\mu}\hat{B} = -\gamma\hat{B}\hat{S} = -\gamma B_0\hat{S}_z - \gamma B_1(\hat{S}_x\cos\omega t - \hat{S}_y\sin\omega t) \quad (5)$$

where $\hat{\mu}$ and γ are the magnetic moment and gyromagnetic ratio of the system, and \hat{S} is the spin operator. Expressing the spin components through the Pauli matrices using $\hat{S}_i = \frac{\hbar}{2}\hat{\sigma}_i$, we finally obtain

$$\hat{H}_I = -\gamma\frac{\hbar}{2}(B_0\hat{\sigma}_z + B_1(\cos\omega t\hat{\sigma}_x - \sin\omega t\hat{\sigma}_y)) \quad (6)$$

This yields for the total Hamiltonian:

$$\hat{H} = \begin{pmatrix} \frac{\hbar\omega_{10}}{2} - \gamma\frac{\hbar}{2}B_0 & -\gamma\frac{\hbar}{2}B_1(\cos\omega t + i\sin\omega t) \\ -\gamma\frac{\hbar}{2}B_1(\cos\omega t - i\sin\omega t) & -\frac{\hbar\omega_{10}}{2} + \gamma\frac{\hbar}{2}B_0 \end{pmatrix} \quad (7)$$

For simplicity, we introduce $A = \frac{\hbar\omega_{10}}{2} - \gamma\frac{\hbar}{2}B_0$ and $B = -\gamma\frac{\hbar}{2}B_1$ and express the oscillating terms using the complex exponential function:

$$\hat{H} = \begin{pmatrix} A & B \cdot e^{i\omega t} \\ B \cdot e^{-i\omega t} & -A \end{pmatrix} \quad (8)$$

From the eigenvalue equation, we get the new energy levels:

$$E_{\pm} = \pm\sqrt{A^2 + B^2} \quad (9)$$

The eigenvectors can now be found from

$$E_{\pm}|\psi_{\pm}\rangle = \hat{H}|\psi_{\pm}\rangle \quad (10)$$

Thus, the components α and β of $|\psi_+\rangle$ have to satisfy

$$(A - \sqrt{A^2 + B^2})\alpha = -\beta B e^{i\omega t} \Leftrightarrow \beta = \frac{\sqrt{A^2 + B^2} - A}{B} e^{-i\omega t} \alpha \quad (11)$$

The normalization requires

$$|\alpha|^2 + |\beta|^2 = \left(\frac{\sqrt{A^2 + B^2} - A}{B} \right)^2 |\alpha|^2 + |\alpha|^2 = 1 \quad (12)$$

By introducing polar coordinates: $\sin \theta = B/\sqrt{A^2+B^2}$, $\cos \theta = A/\sqrt{A^2+B^2}$ this simplifies to

$$1 = |\alpha|^2 \left(1 + \frac{(1 - \cos \theta)^2}{\sin^2 \theta} \right) = |\alpha|^2 \left(\frac{2(1 - \cos \theta)}{\sin^2 \theta} \right) = |\alpha|^2 \frac{1}{\cos^2 \frac{\theta}{2}} \quad (13)$$

$$\Rightarrow |\alpha| = \cos \frac{\theta}{2} \quad (14)$$

As an overall phase can be chosen at will, we set $\alpha = \cos \frac{\theta}{2}$. Equation (11) demands then that $\beta = \sin \frac{\theta}{2} e^{-i\omega t}$, returning the following eigenvector:

$$|\psi_+\rangle = \cos \frac{\theta}{2} |1\rangle + \sin \frac{\theta}{2} e^{-i\omega t} |0\rangle \quad (15)$$

Analogously, we get for the eigenvector for E_- :

$$|\psi_-\rangle = \sin \frac{\theta}{2} |1\rangle - \cos \frac{\theta}{2} e^{-i\omega t} |0\rangle \quad (16)$$

Now we can represent $|0\rangle$ and $|1\rangle$ in the new basis of eigenvectors:

$$|1\rangle = \cos \frac{\theta}{2} |\psi_+\rangle + \sin \frac{\theta}{2} |\psi_-\rangle \quad |0\rangle = e^{i\omega t} \left(\sin \frac{\theta}{2} |\psi_+\rangle - \cos \frac{\theta}{2} |\psi_-\rangle \right) \quad (17)$$

Let the system be in state $|0\rangle$ at the time $t = 0$:

$$|\psi(t=0)\rangle = \sin \frac{\theta}{2} |\psi_+\rangle - \cos \frac{\theta}{2} |\psi_-\rangle \quad (18)$$

The time evolution of this state reads:

$$|\psi(t)\rangle = \sin \frac{\theta}{2} e^{-i\frac{E_+}{\hbar}t} |\psi_+\rangle - \cos \frac{\theta}{2} e^{-i\frac{E_-}{\hbar}t} |\psi_-\rangle \quad (19)$$

The probability of finding the system in state $|1\rangle$ after time t is:

$$\begin{aligned} P_{0 \rightarrow 1}(t) &= |\langle \psi(t) | 1 \rangle|^2 = \left| \sin \frac{\theta}{2} \cos \frac{\theta}{2} \left(e^{-i\frac{E_+}{\hbar}t} - e^{-i\frac{E_-}{\hbar}t} \right) \right|^2 \\ &= 2 \sin^2 \frac{\theta}{2} \cos^2 \frac{\theta}{2} \left(1 - \cos \left(\frac{E_+ - E_-}{\hbar} t \right) \right) = \sin^2 \theta \sin^2 \left(\frac{E_+ - E_-}{2\hbar} t \right) \end{aligned} \quad (20)$$

After plugging in the definitions of $\sin \theta$ and $\cos \theta$ and using that $E_+ - E_- = 2\sqrt{A^2 + B^2}$, this can be rewritten as

$$P_{0 \rightarrow 1}(t) = \frac{A^2}{A^2 + B^2} \sin^2 \left(\frac{\sqrt{A^2 + B^2}}{\hbar} t \right) \quad (21)$$

Now we put in the expressions for A and B and introduce some larmor frequencies:

$$\omega_0 = \gamma B_0, \quad \omega_1 = \gamma B_1 \quad (22)$$

which finally gives us

$$P_{0 \rightarrow 1}(t) = \frac{\omega_1^2}{(\omega_{10} - \omega_0)^2 + \omega_1^2} \sin^2 \left(\frac{\sqrt{(\omega_{10} - \omega_0)^2 + \omega_1^2} t}{2} \right) \quad (23)$$

This result is known as Rabi's formula.

Apparently, a resonant oscillation can be achieved when $\omega_{10} = \omega_0$. In this case,

$$P_{0 \rightarrow 1}(t) = \sin^2 \left(\frac{\omega_1 t}{2} \right) \quad (24)$$

So for a magnetic pulse of length $\omega_1 t = \pi \Leftrightarrow t = \pi/\omega_1$ the systems undergoes a complete transition from the ground state to the excited state. This corresponds to a rotation on the Bloch sphere by an angle of π and is hence called a π pulse. Applying a pulse of only half this length creates a coherent superposition of both states of equal weight, comparable to a rotation by the angle $\pi/2$ and therefore called $\pi/2$ pulse.

1.4 Density matrix

The density operator is defined by

$$\hat{\rho} = |\psi(t)\rangle\langle\psi(t)| \quad (25)$$

This renders for a two-level system:

$$\hat{\rho} = \begin{pmatrix} |\alpha|^2 & \alpha\beta^* \\ \beta\alpha^* & |\beta|^2 \end{pmatrix} \quad (26)$$

The diagonal elements are equivalent to the probabilities of finding the system in state $|0\rangle$ or $|1\rangle$, the normalization requires $\rho_{11} + \rho_{22} = 1$ and therefore they are called *populations*. The off-diagonal elements are called *coherences*[10].

From the Schrödinger equation we obtain[6]

$$i\hbar \frac{\partial \hat{\rho}}{\partial t} = [\hat{H}, \hat{\rho}] \quad (27)$$

Until now, we ignored any relaxation processes caused by spontaneous emission or coupling between the system and its environment. In order to take these effects into account, we introduce the decay rate Γ from the excited state to the ground state. Using equation (27) we can now write in terms of the density matrix:

$$\frac{1}{i\hbar} [\hat{H}_R, \hat{\rho}]_{11} = \frac{-\rho_{11}}{T_1} = -\Gamma \rho_{11} \quad (28)$$

$$\frac{1}{i\hbar} [\hat{H}_R, \hat{\rho}]_{22} = \frac{\rho_{11}}{T_1} = (1 - \rho_{22})\Gamma \quad (29)$$

where \hat{H}_R is the relaxation Hamiltonian and T_1 denotes the lifetime of the excited state and is known as *longitudinal relaxation*. As relaxation needs to be taken into account for the coherences as well, we additionally get

$$\frac{1}{i\hbar}[\hat{H}_R, \hat{\rho}]_{12} = \frac{-\rho_{12}}{T_{12}} = -\gamma\rho_{12} \quad (30)$$

$$\frac{1}{i\hbar}[\hat{H}_R, \hat{\rho}]_{21} = \frac{-\rho_{21}}{T_{21}} = -\gamma\rho_{21} \quad (31)$$

This process is called *transverse relaxation* with the relaxation time $T_{12} = T_{21} = T_2 = \gamma^{-1}$. In order to consider dephasing as well, we introduce the *dephasing time* T_2^* which is the transverse relaxation time modified by a dephasing time. It is [5]

$$2T_1 \geq T_2 \geq T_2^* \quad (32)$$

and for **well prepared** systems with an infinite ground state lifetime and no dephasing, the transverse and longitudinal relaxation are related through

$$\gamma = \frac{1}{2}\Gamma \quad (33)$$

These relaxation processes prevent the system from getting back to the initial amplitude, even if it's excited with a resonant frequency. The observed signal for Rabi oscillations is therefore not a sine but a convolution of a sine with the exponential function.

1.5 Second order correlation function

The intensity correlation function of the light can be found by making two intensity measurements with a fixed time delay τ and averaging the product of the readings. As the normalized form of this function is more useful, the *degree of second-order temporal coherence* is defined as

$$g^{(2)}(\tau) = \frac{\langle \bar{I}(t)\bar{I}(t+\tau) \rangle}{\bar{I}^2} = \frac{\langle E^*(t)E^*(t+\tau)E(t+\tau)E(t) \rangle}{\langle E^*(t)E(t) \rangle^2} \quad (34)$$

where \bar{I} is the averaged intensity[11]. For a single-mode light field, the coherence function at $\tau = 0$ can be expressed in terms of the *destruction* and *creation operators*:

$$g^{(2)}(0) = \frac{\langle \hat{a}^\dagger \hat{a}^\dagger \hat{a} \hat{a} \rangle}{\langle \hat{a}^\dagger \hat{a} \rangle^2} \quad (35)$$

Considering that $[\hat{a}, \hat{a}^\dagger] = 1$ and $\hat{n} = \hat{a}^\dagger \hat{a}$, one gets:

$$g^{(2)}(0) = \frac{\langle n^2 \rangle - \langle n \rangle}{\langle n \rangle^2} \quad (36)$$

A single photon source can be described with a Fock state, for which $\langle n \rangle = n$ and $\langle n^2 \rangle = n^2$, so that follows:

$$g^{(2)}(0) = 1 - \frac{1}{n} \quad (37)$$

1.6 Spin manipulation sequences

In order to examine different NVs and prolong their coherence times, different types of sequences have been applied. The sequences have in common, that they all start with a laser pulse to initiate the system to $m_s = 0$ before the spin manipulation is performed.

1.6.1 Rabi Sequence

The Rabi sequence was used to determine the length of the π -pulse for a specific NV. So the sequence consists of a laser pulse which is long enough to initiate the system to $m_s = 0$ and a RF pulse of length τ . After that, the PL is measured. Measuring the PL for different lengths τ of the MW pulses yields an image of the Rabi Oscillations: An extremum is reached when τ matches a multiple of the length of a π pulse. Therefore, the time interval between two consecutive extrema gives the length of a π pulse for this NV.

1.6.2 Hahn Echo

In the Hahn Echo, a $\pi/2$ pulse is applied to create a coherent superposition of $m_s = 0$ and $m_s = 1$. This state can then evolve over a time τ and inhomogeneities of the magnetic field lead to dephasing. Then, a π pulse turns the polarization around and the spins are refocused again after another time interval τ . At that point, a second $\pi/2$ pulse is applied to map the signal to the readout basis [8] and the PL is measured. As only the static effects cancel each other out, time dependent fluctuations prevent the system from fully getting back to the initial state. For simple spin systems, the PL will decay exponentially with the time τ . The inverse decay rate of the PL thus equals the transverse relaxation time T_2 , as dephasing effects are removed. So, the Hahn Echo pulse sequence allows us to determine the T_2 time.

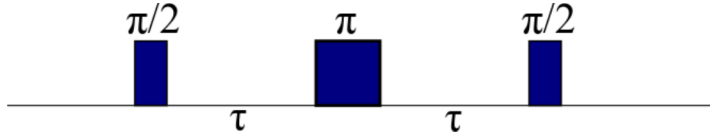


Figure 1: Hahn Echo sequence

1.6.3 Decoupling sequences

The surrounding spin bath of ^{13}C nuclei [4] is the main reason for dephasing of the NV spin and has a huge impact on the coherence time. This mechanism can be circumvented to some extent with specific sequences which decouple the NV spin from interactions with its environment and thereby increase the coherence times.

1.6.3.1 Carr-Purcell-Meiboom-Gill sequence The CPMG sequence begins with a $\pi/2$ rotation around the y axis, followed by a number n of $(\tau - \pi_x - \tau)$ pulses - τ being the relaxation time again - and ends with a $(-\pi/2)_y$ pulse, projecting the spin back to the bright state. The total relaxation time of the NV spin adds up to $T_{rel} = 2n\tau$.

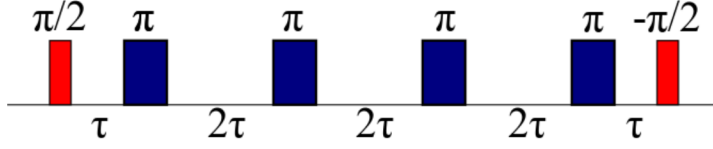


Figure 2: CPMG-4 sequence: red pulses represent rotations around the y-axis, blue pulses are rotations around the x-axis

1.6.3.2 XY sequence As the name implies, the XY sequences is made up of multiple π_x and π_y pulses. They are applied in two different variations: the asymmetric one, starting with an interval τ of free evolution and ending directly after the last pulse; and the symmetric one, which begins and ends with a $\tau/2$ interval. The symmetric sequences have been found to achieve longer coherence times[3][7] and were used in the experiments for this bachelor thesis. In general, the first half of the XY-sequence consists of $(\tau/2 - \pi_x - \tau - \pi_y - \tau/2)$ pulses and in the second part, the order is inverted and the sequence continues with the same number of $(\tau/2 - \pi_y - \tau - \pi_x - \tau/2)$ pulses. As before, the sequence is enclosed by two opposite $(\pi/2)_y$ pulses. With a number n of π pulses again, the total relaxation time turns out to be $T_{rel} = n\tau$.

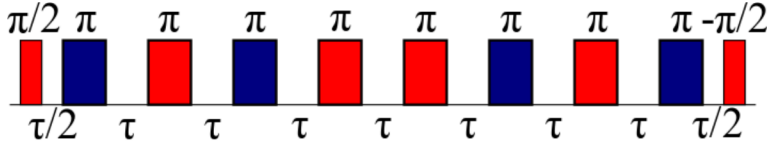


Figure 3: XY-8 sequence

1.6.3.3 UDD sequence Interestingly, equidistant pulse spacings do not always produce the best results with regard to decoupling. So, sequences with n π_x pulses at the time points

$$\delta_j = \tau \sin^2 \left(\frac{\pi j}{2n+2} \right) \quad (38)$$

have proven to achieve the optimum suppression of decoherence caused by imperfect pulses. Furthermore, they perform also well with regard to the decoupling from a spin bath [13]. Between the two required $(\pi/2)_y$ pulses, the sequence is symmetric with increasing time intervals to the middle and decreasing spacings to the end. The total free spin relaxation time of UDD is just τ .

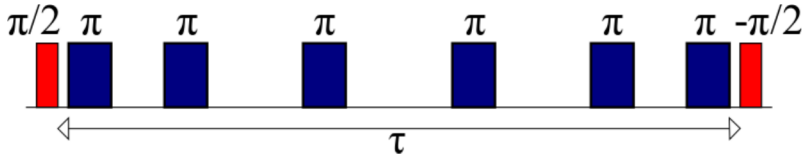


Figure 4: UDD-6 sequence

2 Experiment

2.1 Experimental setup

2.1.1 Optical setup

The first component of the setup is a 532 nm Laser that drives the NVs to $m_s = 0$. The Laser can be pulsed with an AOM. After that, the light goes through a 532 nm shortpass and two collecting lenses with a density filter in between, creating a clear beam of the preferred wavelength. The next element is a dichroic mirror (DM) which lets through green light and reflects red light. Having passed the DM, the beam goes into the microscope and gets focused onto the sample with an objective lens of NA=1.35. The sample is a nanodiamond with multiple NVs and is mounted onto a piezo-controlled xyz stage. A microwave antenna is placed above the sample, allowing us to conduct ESR measurements and run decoupling sequences. The photons emitted by the NVs are collected with the lens before leaving the microscope. At the DM, the red PL gets reflected. A long pass filter removes residual Laser light, before the beam goes into the confocal part that is made up of two collecting lenses and a pinhole in between. At the end, the light reaches the Hanbury-Brown-Twiss setup. This consists of a beam splitter, which has a 50:50 probability of either reflecting or transmitting the photons, and two APDs for counting the reflected and transmitted photons, respectively. Since the APD signals shouldn't be acquired all the time the APDs are gated. This means, that the detected intensity is only read out, when the gates are open. There are two gates: the reference gate (ref), which is open before the spin manipulation took place and the signal gate (sig) which is open at the end of the sequence. Their quotient sig/ref yields the normalized intensity.

The laser and the APD gates are controlled by the bit pattern generator.

2.1.2 Microwave setup

For the purpose of doing various ESR measurements on the NVs, it was essential to use two different microwaves with a relative phase shift of 90° . This could be accomplished in an additional part of the setup. At first, the signal of the RF generator gets into a 0° - 90° RF power splitter. Then, each separate signal goes through a switch that is controlled via TTL pulses from the bit pattern generator. Finally, the signals from both switches are recombined in a simple RF power combiner and transmitted to the microwave antenna. A setup scheme is depicted in figure 5

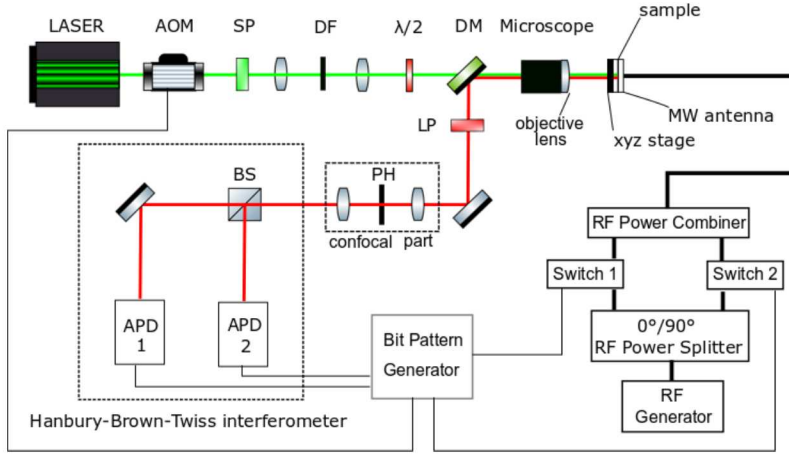


Figure 5: Schematic image of the experimental setup

2.2 Confocal microscopy

A conventional microscope collects all the light which is emitted or reflected by the sample, regardless of whether it originates from the focal plane or not and thus leading to a reduction in contrast and sharpness of the image. The great advantage of a confocal microscope is, that it doesn't only achieve a high 2-D resolution but is also able to suppress light which doesn't come from the focal plane. This can be achieved with a pinhole in a confocal plane. In our setup, it was implemented by putting two collecting lenses in the beam path and placing the pinhole in the mutual focal plane between the two lenses. As only the photons that go through the pinhole are detected, light from below or above the focal plane is extinguished. So, this arrangement accomplishes depth discrimination as shown in figure 6.

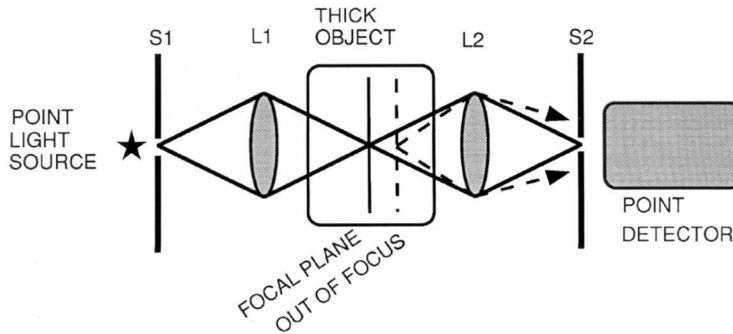


Figure 6: Schematic image of the confocal part of the setup, illustrating depth discrimination with the dashed beams

Apparently, the degree of depth discrimination depends on the size of the pinhole and can consequently be modified by changing the diameter of this aperture. However, in our experiments only the smallest possible hole was used. Furthermore, the confocal part also filters out stray light, hence enhancing the

contrast[9].

2.2.1 Point Spread Function

Due to diffraction effects, light that comes from a point-like object in the focal plane doesn't converge to a single point in the image, but spreads slightly in all directions, even if all optical components have ideal properties and are perfectly adjusted. In confocal fluorescence microscopy, this phenomenon occurs actually twice: the laser light cannot be ideally focused onto the sample, and the emitted light cannot be perfectly focused on the pinhole. The image of a single point can be described by the point spread function (PSF), which accordingly contains information about the highest possible resolution. Since the confocal microscope enables imaging in three dimensions, it is necessary to consider the 3-D PSF, which appears to be a rotational ellipsoid:



Figure 7: Slices through the 3-D PSF. The left image shows the intensity distribution in axial direction and the right image shows a lateral plane

According to the Rayleigh-criterion, two components of equal intensity should be considered to be just resolved when the principal intensity maximum of one coincides with the first intensity minimum of the other[2]. Naturally, resolution is also affected by the signal-to-noise ratio of the system[12], so this criterion cannot be applied in every case. The distance to the first minimum can be conveniently approximated with the *full width at half maximum* (FWHM) of the distribution, so this property will be employed to determine the resolution. Considering the limited resolving power of the objective lens, described by its numerical aperture NA , it is

$$FWHM_z \approx \frac{0.88 \cdot \lambda_{exc}}{\left(n - \sqrt{n^2 - (NA)^2}\right)} \quad (39)$$

for the axial confocal PSF and we get

$$FWHM_{xy} \approx 0.51 \frac{\lambda_{exc}}{NA} \quad (40)$$

for the lateral resolution with λ_{exc} being the excitation wavelength and n the refractive index of the immersion medium. These formulae were derived assuming

that the pinhole is large compared to the diameter of the Airy disc,

$$PH \gg \frac{1.22 \cdot \sqrt{\lambda_{exc} \cdot \lambda_{em}}}{NA} \quad (41)$$

with the emission wavelength λ_{em} , so that additional diffraction could be neglected[9]. After inserting the numbers, equation 41 becomes

$$PH \gg 526.1 \text{ nm} \quad (42)$$

which is well satisfied for the pinhole diameter of 50 μm . So, one gets for the resolution

$$FWHM_z \approx 568 \text{ nm} \quad (43)$$

and

$$FWHM_{xy} \approx 201 \text{ nm} \quad (44)$$

2.3 Calibration

Owing to various lengths of wires and inherent distinctions between the components of the setup, the signals of the bit pattern generator (BPG) don't get to all components at the same time and need different amounts of time to be processed. Consequently, the sequence which is output by the BPG is executed in a completely different way, making it essential to adjust the timing of each element. As just the relative delays of the components to each other needed to be adapted, the delay of the laser was set to zero and the other delays were determined with respect to the laser.

2.3.1 Calibration of the gates

To calibrate the gates, the microscope had to be focused on an NV. Then, the laser was switched on for a short period of time, thereby exciting the NV and producing fluorescence. Simultaneously, the signal and reference gates detected the intensity over the same timespan but with different delays regarding the laser. Thus, the maximum of intensity could be observed when excitation and detection window synchronized, providing the corresponding delay time.

2.3.2 calibration of the microwaves

For the calibration of the microwaves, the laser was turned on for the duration T of the sequence, driving the NV to $m_s = 1$. Additionally, a MW pulse of length τ was applied at time t , the reference was measured from $T/2 - \tau$ until $T/2$ and the signal directly after that, from $T/2$ to $T/2 + \tau$. Then, the signals were measured for different t from 0 to $T - \tau$, shifting the pulse through the sequence. For small t , the normalized intensity would be 1, as the NV is driven back to the excited state by the laser. When t increases further, the counts measured in the reference gate decrease, resulting in a normalized intensity above 1. When the microwave pulse is exactly between the two gates, the normalized intensity reaches 1 again and afterwards, the image is the same as before, just vice versa. So, the microwave is timed correctly, when the normalized intensity goes to 1 exactly at $T/2$.

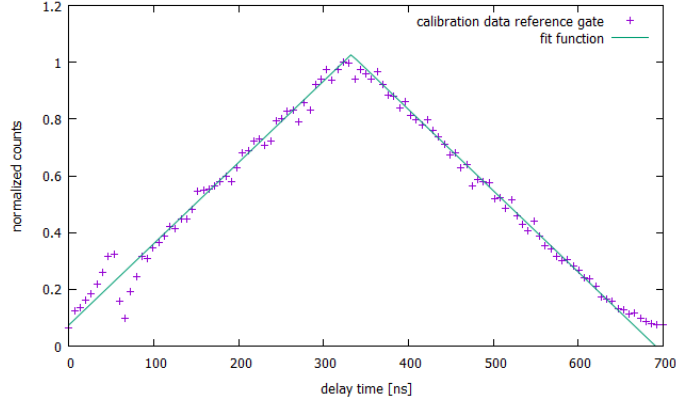


Figure 8: Measurement of the normalized intensity (divided by the maximum value) in dependence of the gate position regarding the laser; the peak of the graph yields the time delay

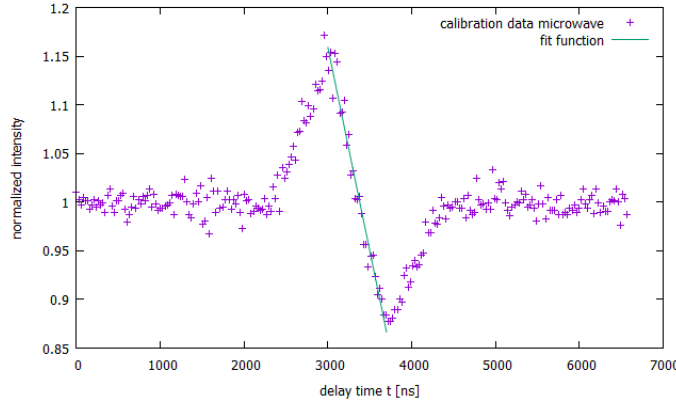


Figure 9: Measurement of the normalized intensity as a function of the mw pulse position

References

- [1] Michel Le Bellac. *A Short Introduction to Quantum Information and Quantum Computation*. Cambridge University Press, 2006.
- [2] Max Born and Emil Wolf. *Principles of Optics*. Pergamon Press, 1970.
- [3] Alexandre M. Souza et al. Effects of time-reversal symmetry in dynamical decoupling. *Physical Review A* 85, 2012.
- [4] C. A. Ryan et al. Robust Decoupling Techniques to Extend Quantum Coherence in Diamond. *Physical Review Letters*, 2010.
- [5] C. Lü et al. Spin relaxation time, spin dephasing time and ensemble spin dephasing time in n-type GaAs quantum wells. *Physics Letters*, 2007.
- [6] Claude Cohen-Tannoudji et al. *Quantum mechanics*. WILEY, 1977.

- [7] M. A. A. Ahmed et al. Robustness of dynamical decoupling sequences. *arXiv:1211.5001v2*, 2012.
- [8] R. Hanson et al. Room-temperature manipulation and decoherence of a single spin in diamond. *Physical Review B* 74, 2006.
- [9] Stefan Wilhelm et al. Die konfokale Laser Scanning Mikroskopie. Technical report, Carl Zeiss Mikroskopsysteme, 2003.
- [10] Malcolm H. Levitt. *Spin dynamics*. WILEY, 2001.
- [11] Rodney Loudon. *The quantum theory of light*. Oxford University Press, 2004.
- [12] Michiel Müller. *Confocal Fluorescence Microscopy*. SPIE Press, 2006.
- [13] Götz S. Uhrig. Exact Results on Dynamical Decoupling by Pi Pulses in Quantum Information Processes. *arXiv:0803.1427v2*, 2008.